BIO Integration

Rapid and Specific Cell-Surface Anchoring of Gold Nanostars for Photoacoustic BMSC Imaging

Graphical abstract

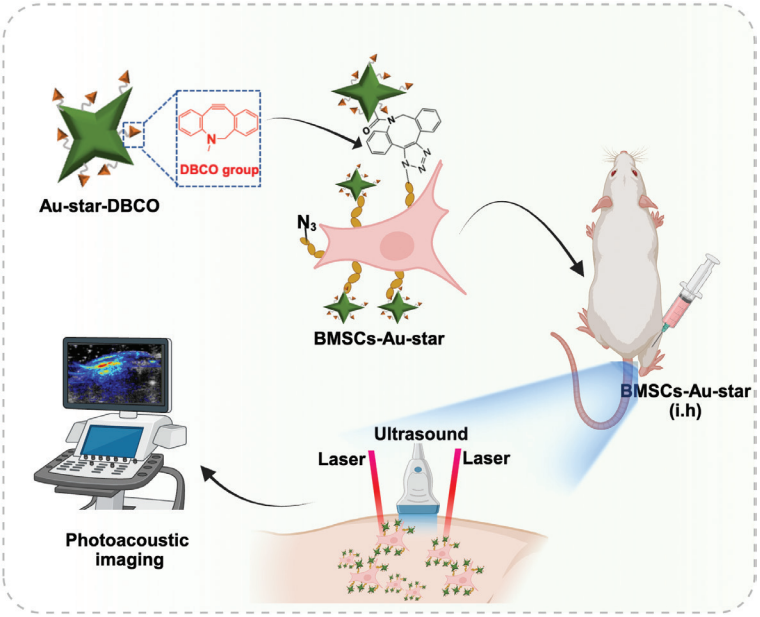

Highlights

- A novel pre-labeling strategy integrates metabolic glycoengineering with copper-free click chemistry to covalently anchor gold nanostars onto BMSC membranes.
- This bioorthogonal method achieves rapid and highly efficient stem cell labeling, thereby overcoming the limitations of traditional endocytosis-based approaches.
- The Au-star-DBCO labeling exhibits excellent biocompatibility, and preserves cell viability and the multi-lineage differentiation ability of BMSCs.
- Labeled BMSCs generate strong, stable photoacoustic signals enabling sensitive, longitudinal *in vivo* tracking for at least 72 hours post-transplantation in a rat model.

Authors

Renhao Xu, Yanmei Cai, Xiaobin Dong, Xuezhi Wang, Wenyi Zheng, Ning Zhang, Yanni He and Hongmei Liu

Correspondence

rhxu0817@jnu.edu.cn (R. Xu);
heyn@gd2h.org.cn (Y. He);
liuhm@gd2h.org.cn (H. Liu)

In brief

This study combined metabolic glycoengineering with bioorthogonal click chemistry to anchor gold nanostars onto BMSC membranes, thereby establishing a platform for rapid and non-invasive photoacoustic imaging. This strategy enables efficient stem cell labeling while preserving cell viability and differentiation ability. The platform facilitates sensitive, longitudinal tracking of transplanted cells *in vivo*. This powerful new tool enables real-time monitoring and precise assessment in stem cell therapy.

Original Article

BIO Integration

Rapid and Specific Cell-Surface Anchoring of Gold Nanostars for Photoacoustic BMSC Imaging

Renhao Xu[1,a,*], Yanmei Cai[1,a], Xiaobin Dong[1], Xuezhi Wang[1], Wenyi Zheng[1], Ning Zhang[1], Yanni He[1,2,*] and Hongmei Liu[1,2,*]

Abstract

Background: Bone marrow mesenchymal stem cell (BMSC) therapy holds great promise for regenerative medicine, but its clinical translation is hindered by the lack of non-invasive, real-time methods to track transplanted cell fate *in vivo*. Although photoacoustic (PA) imaging offers deep-tissue penetration and high sensitivity, existing cell-labeling strategies relying on endocytosis of contrast agents have drawbacks of prolonged incubation times and variable efficiency, thus potentially compromising cell viability and function.

Methods: To address these limitations, we developed a rapid, bioorthogonal pre-labeling strategy. Azide (N_3) groups were first metabolically engineered onto BMSC surfaces. Subsequently, dibenzocyclooctyne (DBCO)-functionalized gold nanostars (Au-star-DBCO) were conjugated to the cells via a highly efficient, copper-free click reaction, thereby enabling covalent membrane anchoring.

Results: This approach achieved rapid and specific stem cell labeling within 3 h, with an efficiency of 83.1% ± 0.67. The labeling process did not impair BMSC viability or multilineage differentiation potential. The Au-star-DBCO-labeled BMSCs generated strong, concentration-dependent PA signals both *in vitro* and in a rat subcutaneous model, and enabled dynamic monitoring for at least 72 h post-transplantation. The specificity of the bioorthogonal reaction provided a significantly higher signal-to-noise ratio than passive uptake methods.

Conclusions: We successfully established a biocompatible and efficient platform for stem cell tracking by integrating metabolic glycoengineering, bioorthogonal chemistry, and nanostar-enhanced PA imaging. This strategy overcomes key limitations of traditional endocytosis-based labeling, and offers a rapid, specific, and functional cell-compatible tool for sensitive, longitudinal *in vivo* monitoring. This platform may advance precise assessment of cell therapies and facilitate their clinical application.

Keywords

Bone marrow mesenchymal stem cells, gold nanostars, photoacoustic.

Introduction

Cell therapy has emerged as a cutting-edge direction in regenerative medicine and disease treatment [1, 2]. By transplanting functional cells to repair or replace damaged tissues, cell therapy offers novel therapeutic strategies for a variety of refractory diseases [3, 4]. Notably, bone marrow mesenchymal stem cells (BMSCs) have demonstrated substantial potential in preclinical research and early-stage clinical trials for numerous conditions, including bone and joint diseases, neurodegenerative diseases, myocardial injury, and autoimmune diseases [5, 6]. This promise has been attributed to their advantages including multipotent differentiation capability, potent paracrine functions, and low immunogenicity [7, 8]. However, the successful clinical translation of stem cell therapy faces a critical bottleneck in methods for tracking the fate of transplanted cells non-invasively, in real time, and longitudinally within living organisms, including cell distribution, migration, survival, and differentiation behaviors [9, 10]. The lack of such tracking capability severely limits understanding of therapeutic mechanisms, dosage optimization, and safety assessment. Therefore, developing efficient, sensitive, and biocompatible cell labeling and *in vivo* tracking technologies will be crucial for advancing the precision and standardization of cell therapy.

Among various *in vivo* imaging modalities, ultrasound imaging is widely used in clinical settings and has been explored for tracking microbubble-labeled cells, because of its advantages of real-time capability, high spatiotemporal resolution,

[1]Department of Ultrasound, Institute of Ultrasound in Musculoskeletal Sports Medicine, The Affiliated Guangdong Second Provincial General Hospital of Jinan University, Guangzhou 510317, China

[2]Guangdong Engineering Technology Research Center of Emergency Medicine, Guangzhou 510317, China

[a]These authors contributed equally to this work.

*Correspondence to: Renhao Xu, Department of Ultrasound, Institute of Ultrasound in Musculoskeletal Sports Medicine, The Affiliated Guangdong Second Provincial General Hospital of Jinan University, Guangzhou 510317, China, E-mail: rhxu0817@jnu.edu.cn; Yanni He, Department of Ultrasound, Institute of Ultrasound in Musculoskeletal Sports Medicine, The Affiliated Guangdong Second Provincial General Hospital of Jinan University, Guangdong Engineering Technology Research Center of Emergency Medicine, Guangzhou 510317, China, E-mail: heyn@gd2h.org.cn; Hongmei Liu, Department of Ultrasound, Institute of Ultrasound in Musculoskeletal Sports Medicine, The Affiliated Guangdong Second Provincial General Hospital of Jinan University, Guangdong Engineering Technology Research Center of Emergency Medicine, Guangzhou 510317, China, E-mail: liuhm@gd2h.org.cn

Received: January 20 2026
Revised: February 27 2026
Accepted: March 9 2026
Published Online: April 1 2026

Available at: https://bio-integration.org/

lack of radiation, and low cost [11, 12]. Previous studies, including work from our team, have confirmed that loading nanobubbles into stem cells or immune cells via biosynthetic or physical methods can achieve ultrasound contrast enhancement and tracking [13, 14]. However, because it typically requires prolonged incubation times (often exceeding 24 h) for effective cellular uptake, this approach has low efficiency. More importantly, microbubbles undergo acoustic cavitation and rupture under ultrasound exposure, thus leading to irreversible signal loss and precluding long-term, repeated imaging monitoring.

In recent years, photoacoustic (PA) imaging has emerged as a promising hybrid imaging technique combining the contrast of optical imaging with the deep penetration of ultrasound [15, 16]. Unlike conventional ultrasound imaging, which relies on mechanical acoustic properties, PA imaging generates images by detecting ultrasound signals produced when tissues absorb pulsed laser light, thereby providing molecular and functional information based on optical absorption. Importantly, some nanomaterials with strong near-infrared absorption, such as Prussian blue nanoparticles, gold nanorods, and gold nanostars (Au-stars), serve as excellent PA contrast agents [17, 18]. Via cellular endocytosis, these nanomaterials have been used for PA labeling and tracking of stem cells [19]. For stem cell tracking, probe biocompatibility is critical. The biosafety of gold-based nanomaterials has been well established in previous studies [20, 21]. Au-stars offer substantial advantages, because they can be rapidly synthesized with only Good's buffers, which serve as both reducing and capping agents, thereby avoiding the need for toxic surfactants such as Cetyltrimethylammonium bromide (CTAB) [22]. However, because existing strategies rely predominantly on the passive biological process of phagocytosis, labeling efficiency is highly dependent on cell type and state, and lengthy incubation times (typically 12–48 h) are necessary. The prolonged labeling process not only affects cell viability and function but also prevents application of this technology in clinical scenarios requiring rapid preparation of cellular products. Consequently, an urgent need exists to develop a rapid, efficient PA labeling method that does not compromise cell viability, to broaden the application scope of stem cell PA imaging and accelerate its clinical translation.

Bioorthogonal chemical reactions offer a highly promising tool to address these challenges [23]. These reactions can proceed efficiently and specifically under physiological conditions without interfering with inherent biochemical processes, and they exhibit excellent biocompatibility [24]. Among them, the copper-free click reaction between dibenzocyclooctyne (DBCO) and azide groups has been widely applied in bioconjugation and cell labeling [25]. In addition, Au-star materials are considered ideal nanoprobes for PA imaging, because of their small size (typically <50 nm), large near-infrared absorption cross-section, high photothermal conversion efficiency, strong PA signal, simple synthesis, and high reproducibility [22]. Consequently, this study was aimed at developing a novel pre-labeling strategy in which azide groups (N_3) were first introduced onto the surfaces of BMSC membranes via metabolic glycoengineering technology, and a subsequent rapid bioorthogonal click reaction with DBCO-modified Au-stars (Au-star-DBCO) achieved efficient, covalent membrane-surface labeling of stem cells (**Figure 1**). This method was designed to overcome the limitations of traditional endocytosis-dependent labeling, substantially shorten labeling time, and enhance labeling specificity and stability. This efficient, versatile, and rapid PA labeling platform was demonstrated to have minimal effects on cell function. Therefore, this platform has promise in enabling sensitive, dynamic, and long-term monitoring of cell therapy processes *in vivo*, and providing powerful technical support for optimizing cell therapy protocols and advancing their clinical evaluation.

Materials and methods

Key reagents

DBCO-PEG-SH (M.W. 2000 Da) was purchased from JinXinBio (Guangzhou, China). Chloroauric acid ($HAuCl_4$) and 4-(2-hydroxyethyl)piperazine-1-ethanesulfonic acid (HEPES) were obtained from Aladdin (Shanghai, China). DBCO-Cy5, rhodamine-PEG-SH (M.W. 3400 Da), and Peracetylated N-azidoacetylmannosamine (Ac_4ManNAz) were purchased from MedChemExpress (Shanghai, China). All cell culture media were acquired from Gibco (Rockville, USA). A Cell Counting Kit-8 (CCK-8), alizarin red staining kit, alcian blue staining kit, Oil Red O staining kit, and Hoechst dye were purchased from Beyotime Biotechnology (Shanghai, China). Osteogenic, adipogenic, and chondrogenic induction differentiation media were obtained from Cyagen (Suzhou, China).

Preparation of Au-star, Au-star-DBCO, and rhodamine-Au-star-DBCO

Au-stars were synthesized with a seedless method, as previously described [22]. Briefly, 750 μL of 1 M HEPES buffer (pH 7.4) was added to 9.05 mL ultrapure water, and 0.2 mL 10 mM $HAuCl_4$ was subsequently added. A stir bar was immediately introduced, and the mixture was stirred for 30 s at 1000 rpm, then left undisturbed for 2 h. The resulting Au-stars were centrifuged and washed three times at 8000 rpm. For quantification, 100 μL Au-star solution was digested with aqua regia and analyzed with inductively coupled plasma mass spectrometry (Optima 2000 DV).

For the synthesis of Au-star-DBCO, 10 mL 10 mM Au-star solution was mixed with 1 mM DBCO-PEG-SH and stirred at room temperature for 6 h at 600 rpm. The product was then centrifuged, washed with ultrapure water, and resuspended in 1 mL PBS.

Rhodamine-labeled Au-star-DBCO (rhodamine-Au-star-DBCO) was prepared similarly, by the addition of 1 mM DBCO-PEG-SH and 200 μM rhodamine-PEG-SH to 10 mL 10 mM Au-star solution, followed by stirring at room temperature for 6 h at 600 rpm. The product was centrifuged, washed with ultrapure water, and resuspended in 1 mL PBS.

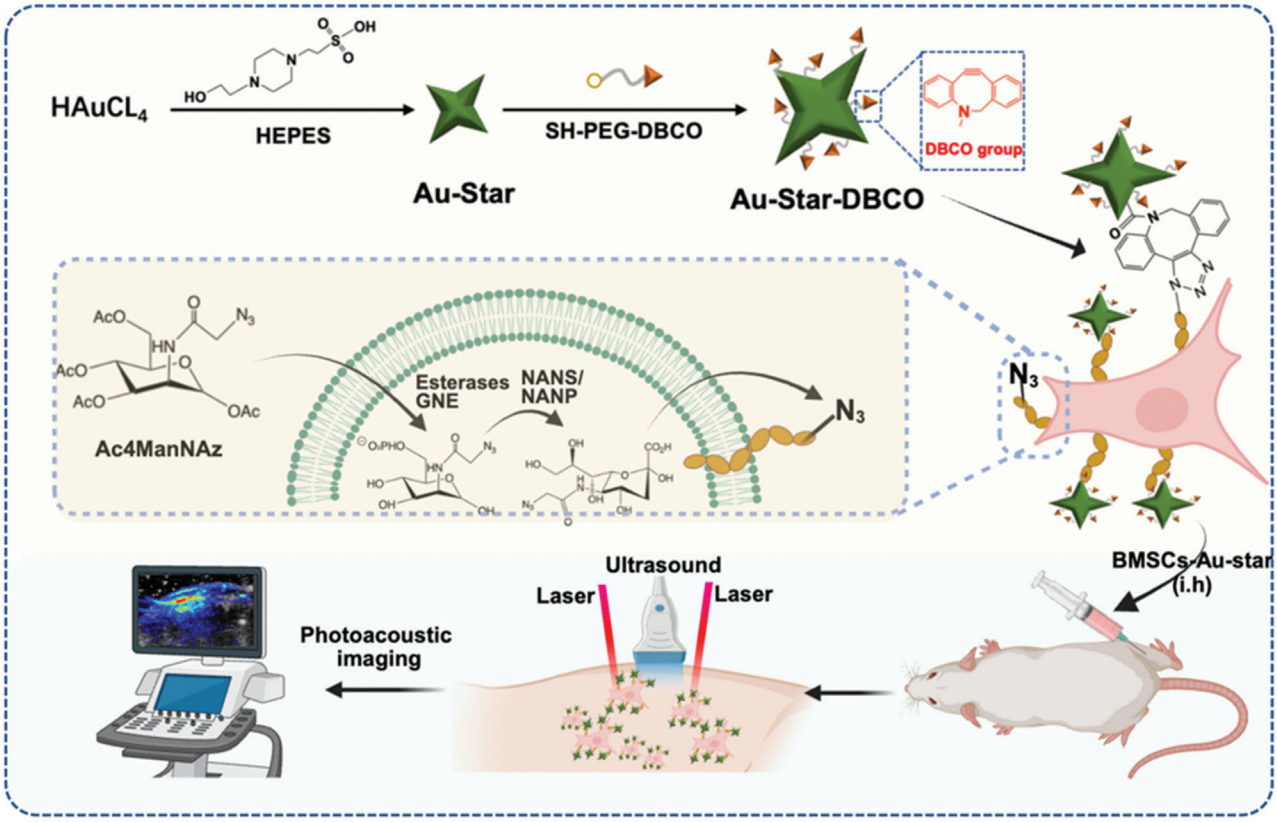

Figure 1 Schematic diagram of rapid nanogold labeling via bioorthogonal reactions for stem cell photoacoustic imaging.

Characterization of Au-star and Au-star-DBCO

The morphology of Au-star and Au-star-DBCO was examined with transmission electron microscopy (TEM) (JEM-1400Flash; JEOL, Tokyo, Japan). UV-vis spectrophotometry (Cary 5000 spectrophotometer; Agilent, Santa Clara, CA, USA) and infrared spectroscopy (Nicolet iS10; Thermo Fisher Scientific, Waltham, MA, USA) were used to confirm the successful conjugation of DBCO groups onto the Au-star surface. Subsequently, Au-star-DBCO (100 μM) was mixed with Ac_4ManNAz (100 μM), and the reaction was continuously monitored with UV-vis spectrophotometry for 2 min.

Biocompatibility of Au-star-DBCO

The hemocompatibility of Au-star-DBCO was evaluated at concentrations of 50, 100, 200, and 400 μM. Fresh rat blood was collected in heparinized tubes and centrifuged to isolate red blood cells (3000 rpm, 10 min). The purified red blood cells were diluted to 10% (v/v) in PBS, and 200 μL aliquots were mixed with 1 mL test solutions. After incubation at 37°C for 5 h, the samples were centrifuged (3000 rpm, 10 min), and 100 μL supernatant was transferred to a 96-well plate. Absorbance was measured at 540 nm with a microplate reader. The hemolysis percentage was calculated as follows: $[(OD_{sample} - OD_{negative})/(OD_{positive} - OD_{negative})] \times 100\%$.

BMSC isolation and culture

BMSCs were harvested from the bone marrow of 2-week-old male SD rats (Ruige, Guangzhou, China), as previously described [7]. Briefly, femurs and tibiae were aseptically dissected, and bone marrow was flushed with alpha-MEM supplemented with 10% fetal bovine serum and 1% penicillin/streptomycin. The resulting cell suspension was filtered through a cell strainer and cultured in an incubator. The medium was replaced every 8 h to remove non-adherent cells. After 3 days, the cells were passaged and expanded for three or four passages before use in subsequent experiments.

Preparation of BMSCs-N_3

BMSCs were labeled with azide groups via metabolic glycoengineering, as previously described, thus yielding BMSCs-N_3. Briefly, BMSCs were seeded in six-well plates at a density of 2×10^5 cells per well. After 12 h of attachment, the cells were treated with 50 μM Ac_4ManNAz for 24 h. After incubation, the cells were washed three times with PBS to obtain BMSCs-N_3. To verify azide group labeling, we seeded 5×10^4 BMSCs-N_3 in confocal dishes and, after 12 h of attachment, incubated them with 100 μM DBCO-Cy5 for 30 min. The cells were then washed twice with PBS, stained with Hoechst for nuclei visualization, and imaged with a confocal microscope (Stellaris, Leica, Germany).

Cytotoxicity assays

BMSCs were seeded in 96-well plates at a density of 1×10^4 cells per well and treated with various concentrations of Au-star-DBCO (12.5, 25, 50, 100, 200, 400, 600, 800, or 1000 μM) for 24 h or 72 h. Cell viability was assessed with CCK-8 assays, and absorbance was measured at 450 nm with a microplate reader (ELx800, BioTek, USA).

BMSCs-N_3 were seeded under the same conditions and treated with Au-star-DBCO at concentrations of 6.25, 12.5, 25, 50, 100, 200, 400, or 600 μM for 24 h, then subjected to CCK-8 assays and absorbance measurement at 450 nm.

BMSC labeling efficiency assays

BMSCs were seeded in six-well plates at a density of 2×10^5 cells per well. After 12 h of attachment, the cells were treated with 50 μM Ac_4ManNAz for 24 h to generate BMSCs-N_3. The cells were then incubated with 400 μM rhodamine-Au-star-DBCO for various durations (0.5, 1, 3, 6, or 12 h), washed three times with PBS, and analyzed with flow cytometry to determine labeling efficiency.

For confocal imaging, 5×10^4 BMSCs-N_3 were seeded in confocal dishes and, after 12 h of attachment, were incubated with 400 μM rhodamine-Au-star-DBCO for 3 h. The cells were washed twice with PBS, stained with Hoechst, and imaged with a confocal microscope (Stellaris, Leica, Germany).

Preparation and characterization of BMSCs-Au-star

BMSCs were seeded in six-well plates at a density of 2×10^5 cells per well. After 12 h of attachment, the cells were treated with 50 μM Ac_4ManNAz for 24 h to generate BMSCs-N_3. The cells were then incubated with 400 μM Au-star-DBCO for 3 h to obtain Au-star-labeled BMSCs (BMSCs-Au-star). The cellular morphology and distribution of Au-stars on the cell surfaces were examined with TEM.

In vitro BMSC differentiation

BMSCs and BMSCs-Au-star were induced to differentiate toward osteogenic, chondrogenic, and adipogenic lineages with specific induction media. After 21 days of induction, Oil Red O staining, alizarin red staining [26], and alcian blue staining [14] were used to visualize lipid droplets, calcium deposits, and chondrocytes, respectively.

In vitro photoacoustic imaging of Au-star and BMSCs-Au-star

A Vevo F2 system (Fuji VisualSonics, Canada) equipped with a linear array transducer (15–29 MHz frequency) was used to evaluate the photoacoustic imaging performance of Au-star at concentrations of 12.5, 25, 50, 100, 200, 400, and 800 μM. A laser excitation wavelength of 750 nm was selected. For BMSCs-Au-star imaging, 1×10^6 BMSCs were seeded in a 10 cm^2 culture dish and treated with 50 μM Ac_4ManNAz for 24 h to generate BMSCs-N_3. The cells were then incubated with 400 μM Au-star-DBCO for 3 h. Various groups of cells were diluted to concentrations of 6.25×10^4, 12.5×10^4, 25×10^4, 50×10^4, 100×10^4, or 200×10^4 cells/mL, then imaged with the Vevo F2 system.

In vivo photoacoustic imaging of BMSCs-Au-star

All animal procedures were approved by the Ethics Committee of Guangdong Second Provincial General Hospital (animal ethics ID 2025-DW-KZ-116-01). Six-week-old rats were shaved on the thigh area, and 1×10^6 BMSCs or BMSCs-Au-star were subcutaneously injected into the thigh. Photoacoustic images were acquired at various time points (0, 6, 12, 24, or 72 h) post-injection.

Statistical analysis

All experiments were performed in at least three independent replicates, and data are presented as mean ± standard deviation. Statistical significance between the control and treatment groups was determined at $P < 0.05$ (****$P < 0.0001$, ***$P < 0.001$, **$P < 0.01$, and *$P < 0.05$).

Results

Design and characterization of Au-star-DBCO

We synthesized star-shaped Au-stars through a one-pot method with Good's buffer (HEPES). Thiolated PEG-DBCO (DBCO-PEG-SH) was subsequently conjugated to the Au-stars to successfully prepare Au-star-DBCO (**Figure 2A**). UV-vis spectroscopy of Au-star, Au-star-DBCO, and DBCO-PEG-SH (**Figure 2B**) revealed that Au-star-DBCO exhibited the characteristic absorption peak of the DBCO group in the 300–350 nm range, thus confirming successful conjugation of DBCO-PEG-SH to the Au-star surface. Furthermore, Au-star-DBCO showed a distinct absorption peak in the near-infrared region at 750 nm, which was attributed to strong local field enhancement and a resonance redshift caused by the sharp tips of the nanostars. TEM imaging indicated that DBCO modification did not significantly alter the morphology of the Au-stars; both Au-star and Au-star-DBCO maintained their star-shaped structures, with a size of approximately 30–50 nm (**Figure 2C**). Further confirmation was obtained from the infrared spectrum of Au-star-DBCO, which showed a characteristic stretching vibration at 1700–1750 cm^{-1}, corresponding to the C=O group of DBCO (**Figure 2D**). We additionally used UV spectroscopy to monitor the reaction kinetics between Au-star-DBCO and

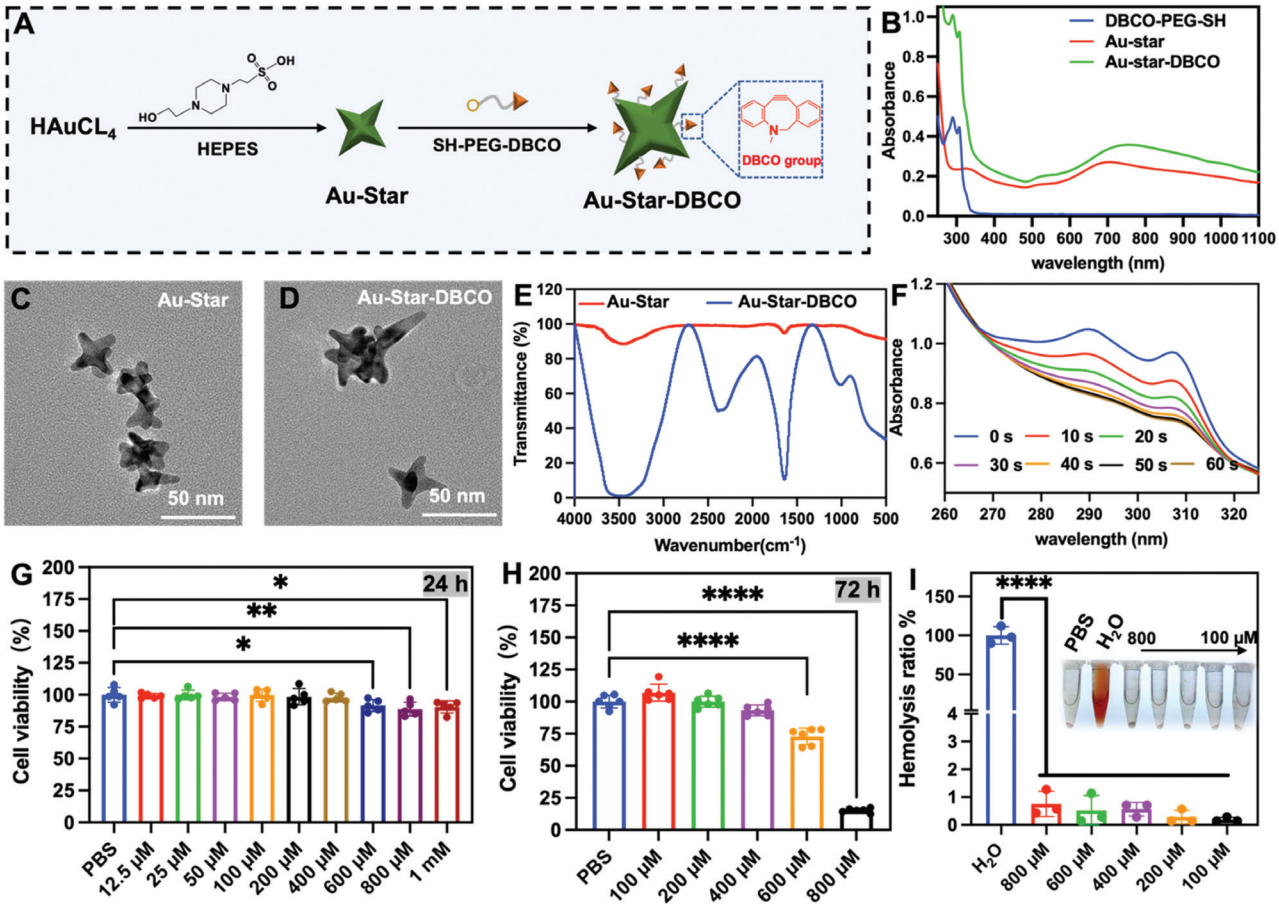

Figure 2 Characterization of Au-star-DBCO. A) Schematic of the synthesis of Au-star-DBCO. B) UV-vis spectra of DBCO-PEG-SH, Au-star, and Au-star-DBCO. C, D) TEM images of Au-star and Au-star-DBCO. E) FTIR spectra of Au-star and Au-star-DBCO. F) UV-vis spectroscopic monitoring of the reaction between Au-star-DBCO and Ac_4ManNAz. G, H) Viability of BMSCs incubated with various concentrations of Au-star-DBCO for 24 h and 72 h. I) Hemocompatibility evaluation of Au-star-DBCO at various concentrations.

peracetylated N-azidoacetylmannosamine [7], thereby further confirming the surface reactivity of the DBCO groups (**Figure 2E, F**).

We next evaluated the effects of Au-star-DBCO on BMSC viability. After 24 h or 72 h co-incubation, significantly greater cytotoxicity was observed with Au-star-DBCO concentrations of ≥600 μM than the PBS control (**Figure 2G, H**). Hemolysis assays using various Au-star-DBCO concentrations demonstrated excellent hemocompatibility (**Figure 2I**).

Bioorthogonal reaction enables rapid labeling of BMSCs

BMSCs were selected for this study because of their crucial roles in tissue repair and regeneration [27, 28]. Co-incubation of Au-star-DBCO with azide-labeled stem cells enabled rapid generation of BMSCs-Au-star (**Figure 3A**). First, BMSCs were treated with Ac_4ManNAz, which is metabolically incorporated into cell surface glycans, thus introducing azide groups. To confirm successful azide labeling, we reacted BMSCs-N_3 with DBCO-Cy5. Fluorescence imaging revealed distinct red fluorescence on BMSCs-N_3, thereby confirming the bioorthogonal reaction between DBCO and the cell-surface azide groups (**Figure 3B**).

We then assessed the effects of various Au-star-DBCO concentrations on the viability of BMSCs-N_3. A concentration of 400 μM significantly inhibited the viability of BMSCs-N_3 (**Figure 3D**). Therefore, a concentration of 200 μM Au-star-DBCO was used for subsequent labeling experiments. Rhodamine-Au-star-DBCO was incubated with BMSCs-N_3 and naive BMSCs for various durations, and labeling efficiency was analyzed with flow cytometry. Owing to the highly efficient bioorthogonal reaction between DBCO and N_3, 83.9% of BMSCs-N_3 were labeled after 3 h of incubation (**Figures 3E, F and S1**). In contrast, naive BMSCs, relying solely on endogenous phagocytic activity, showed only 21.7% positive labeling. Further fluorescence observation confirmed the binding, with distinct red fluorescence surrounding BMSCs-N_3 (**Figures 3C and S2**). Furthermore, cytoskeletal staining (**Figure S3**) indicated that the attachment of Au-stars to the surface of BMSCs did not affect cell morphology or cell spreading. TEM imaging of various groups (**Figure 3G**) revealed no Au-star-DBCO on the cell membranes of the BMSCs + Au-star-DBCO group. In contrast, the BMSCs-N_3 + Au-star-DBCO group clearly showed a high density of Au-star-DBCO on the cell

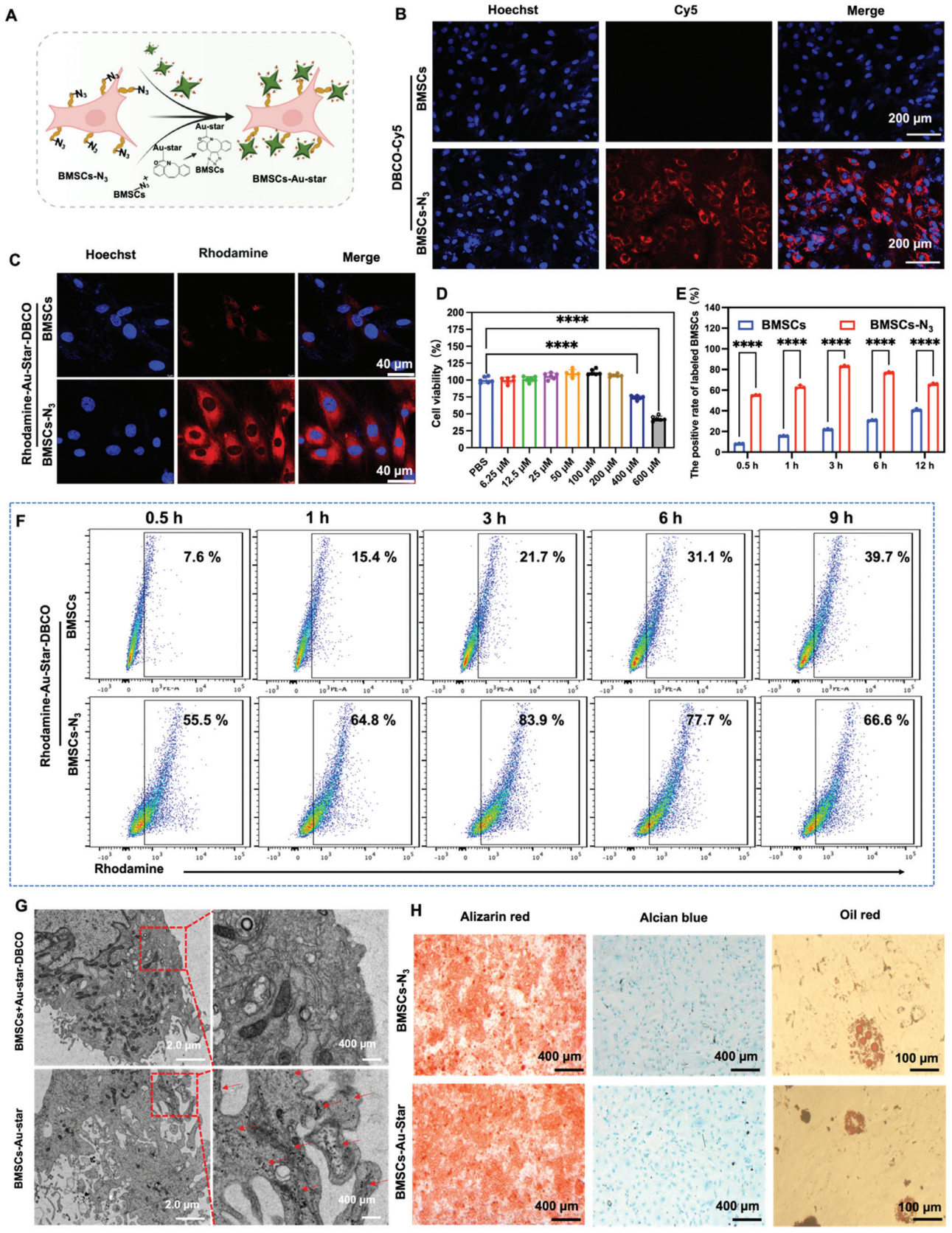

Figure 3 A) Schematic diagram of Au-star-DBCO labeling of BMSCs-N_3. B) Detection of azide (N_3) distribution (red) on the surfaces of BMSCs with fluorescence microscopy. C) Fluorescence image of BMSCs-N_3 and BMSCs incubated with rhodamine-Au-star-DBCO (red), followed by co-staining with Hoechst. D) Influence of various concentrations of Au-star-DBCO on the activity of BMSCs-N_3. E) Quantification of Au-star-DBCO labeling efficiency on BMSCs. F) Flow cytometric analysis of Au-star-DBCO binding to BMSCs via bioorthogonal conjugation. G) TEM images of BMSCs + Au-star-DBCO and BMSCs-N_3 + Au-star-DBCO, showing Au-star attachment to BMSC surfaces through the rapid click response of DBCO and N_3. Red arrows indicate Au-star. H) Representative images of BMSCs-N_3 and BMSCs-Au-star stained with alizarin red, alcian blue, and Oil Red O, indicating the presence of adipocytes, osteoblasts, and cartilage.

membrane, thus further confirming that the bioorthogonal reaction enabled rapid and specific labeling of stem cells with Au-stars.

To investigate whether Au-star labeling might affect the pluripotency of BMSCs, we cultured BMSCs-Au-star in osteogenic, adipogenic, and chondrogenic induction media. Staining with alizarin red (osteogenesis), Oil Red O (adipogenesis), and alcian blue (chondrogenesis) indicated no significant impairment in differentiation potential with respect to unlabeled controls (**Figure 3H**).

In vitro and *in vivo* photoacoustic imaging of BMSCs-Au-star

Given the Au-stars' unique tip structure and strong near-infrared absorption, we explored their PA imaging performance and their ability to enable stem cell tracking. First, PA imaging of Au-star-DBCO and unmodified Au-star at the same concentration confirmed that DBCO-PEG-SH modification did not diminish the PA signal (**Figure 4A**). The PA signal intensity decreased progressively with decreasing Au-star-DBCO concentration (**Figure 4B, C**; change in the material's own color in **Figure S4**). Next, we evaluated the PA imaging of BMSCs after co-incubation with Au-star-DBCO under various conditions. No significant PA signal was detected from naive BMSCs even at high cell concentrations (**Figure 4D, E**). In the Au-star-DBCO + BMSCs-N_3 group, a distinct PA signal was detectable at a cell concentration as low as 12.5×10^4 cells/mL, and the signal intensified with increasing cell concentration. Although a PA signal was also detected in the Au-star-DBCO + BMSCs group, it was significantly weaker than that in the Au-star-DBCO + BMSCs-N_3 group.

To further assess the *in vivo* imaging capability of BMSCs-Au-stars, we subcutaneously injected BMSCs and BMSCs-Au-star into the thigh in rats (**Figure 4F**). PA signals at the injection site were monitored at 0, 6, 12, 24, and 72 h post-injection. Compared with the BMSC control group, the BMSC-Au-star group exhibited a strong, clustered PA signal, indicating local retention of the labeled stem cells. Over time, the PA signal at this site gradually decreased but remained significantly stronger than that in the control group at all time points (**Figure 4G, H**).

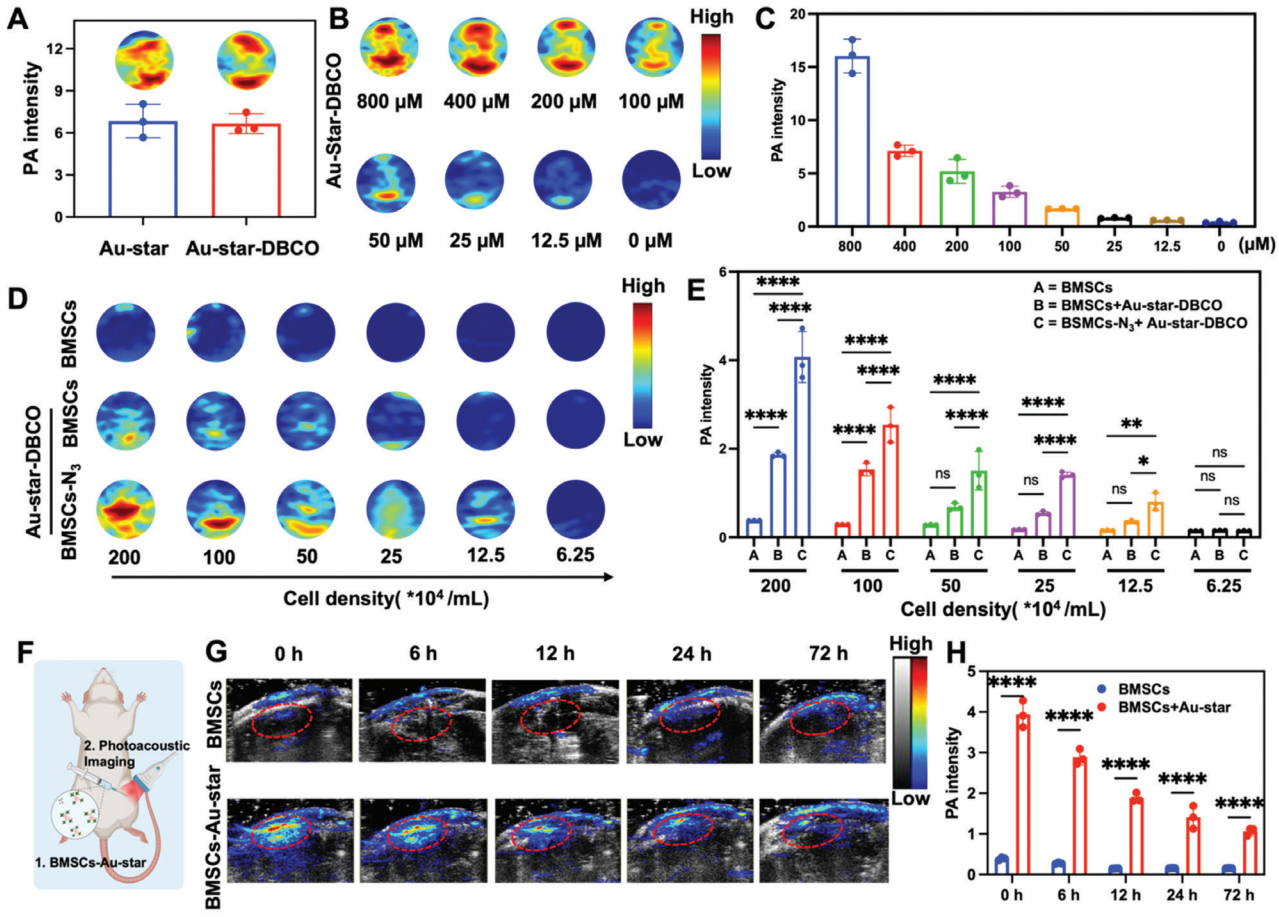

Figure 4 *In vivo* and *in vitro* photoacoustic imaging of BMSCs-Au-star. A) Photoacoustic images of Au-star before and after modification with DBCO-PEG_{2000}-SH. B) Photoacoustic images of Au-star-DBCO at various concentrations. C) Quantitative photoacoustic intensity of Au-star-DBCO across various concentrations. D) Photoacoustic images of BMSCs, BMSCs mixed with Au-star-DBCO, and BMSCs-N_3 labeled with Au-star-DBCO at various concentrations. E) Quantitative photoacoustic intensity of BMSCs, BMSCs mixed with Au-star-DBCO, and BMSCs-N_3 labeled with Au-star-DBCO. F) Schematic diagram of subcutaneous photoacoustic imaging of BMSCs-Au-star in rat hindlimbs. G) *In vivo* photoacoustic images of BMSCs-Au-star under the subcutaneous tissue of rat hindlimbs at various time points. H) Quantitative analysis of subcutaneous photoacoustic signals from BMSCs-Au-star in rat hindlimbs over time.

Discussion

In recent years, stem cell therapy has remained a major research focus, yet its clinical translation has been significantly hindered by the limited ability to visualize and quantitatively track the fate of transplanted cells *in vivo* [13]. This study developed a novel platform based on Au-stars and bioorthogonal click chemistry. Through integration of metabolic glycan engineering with bioorthogonal click reactions, near-infrared-absorbing Au-star-DBCO conjugates were efficiently and covalently anchored onto the BMSC membrane surface, thus enabling highly sensitive photoacoustic imaging and dynamic monitoring of stem cells. Our results indicated successful synthesis of DBCO-functionalized Au-stars, which retained excellent near-infrared optical properties. Moreover, BMSCs metabolically labeled with azide groups underwent a highly efficient and rapid bioorthogonal reaction with Au-star-DBCO and achieved a labeling efficiency of 83.9% within 3 h, with the label primarily localized to the cell membrane. Notably, at effective concentrations, this labeling strategy did not compromise the viability or multilineage differentiation potential of BMSCs. Finally, both *in vitro* studies and a rat subcutaneous transplantation model confirmed that the BMSCs-Au-star generated strong, concentration-dependent photoacoustic signals allowing for longitudinal monitoring for at least 72 h *in vivo*.

Notably, we provide a novel solution to the longstanding challenge of *in vivo* stem cell tracking, by achieving high efficiency, high specificity, and excellent biocompatibility. First, the highly efficient bioorthogonal reaction between DBCO and N_3 served as the basis for specific labeling. Second, the covalent membrane anchoring, coupled with the superior near-infrared absorption properties of the Au-nanostar material, contributed to a stable and strong imaging signal. Finally, the favorable biocompatibility of the nanomaterial supports the applicability of this technique. Notably, we detected a weak photoacoustic signal (21.7% labeling efficiency) in the control group without N_3 labeling, in agreement with expectations based solely on passive cellular uptake mechanisms. This background signal precisely highlights the specificity advantage conferred by the bioorthogonal reaction, which improved the signal-to-noise ratio by approximately fourfold and required only 3 h. Although the labeling efficiency decreased after 6 h of incubation, it remained substantially higher than that observed in the control group. This attenuation might be partly attributable to the epitope dilution effect caused by cell division, given the proliferative activity of stem cells. Furthermore, the finding that stem cell pluripotency was unaffected after labeling crucially indicated the non-invasive nature of this method, representing a core advantage that enables robust labeling while maximally preserving the therapeutic functionality of the cells.

Compared with traditional stem cell tracking methods, the stem cell labeling achieved herein is not only highly efficient but also enables real-time dynamic imaging [29]. In contrast to fluorescent protein or dye labeling, the photoacoustic signal from Au-stars is resistant to quenching and offers greater tissue penetration, thereby addressing challenges in long-term tracking and deep-tissue imaging [30, 31]. Compared with MRI tracking based on superparamagnetic iron oxide nanoparticles, our photoacoustic imaging approach offers higher sensitivity [32]. Moreover, the size and surface engineering of Au-stars facilitate specific membrane anchoring rather than non-specific endocytosis [33]. The key advancement of this work, compared with previous studies using gold nanoparticles for stem cell labeling, is our introduction of a pre-targeting bioorthogonal chemical strategy [22], which transforms labeling from a passive, slow, and incomplete phagocytic process into an active, rapid, and thorough reaction essential for high-efficiency and high-specificity labeling. Therefore, our study, rather than merely applying a nanomaterial for cell labeling, integrated three cutting-edge technologies (metabolic labeling, click chemistry, and nano-photoacoustic probes) through a sophisticated chemical biology design, thus providing a synergistic system with significantly optimized performance.

This study has several limitations that should be addressed in future work. 1) The validation was performed in only a subcutaneous model in healthy rats, which lacked the complexity of actual disease microenvironments. This simplicity might have affected stem cell survival, migratory behavior, and nanoparticle stability. 2) Because the current photoacoustic signal analysis is semi-quantitative, the absolute number of cells *in vivo* is difficult to determine accurately. 3) Key practical issues for future translation remain unresolved. These include whether the concentration of Ac_4ManNAz and its incubation time are optimal for all stem cell types, as well as the processes required for large-scale, clinical-grade production of Au-star-DBCO.

On the basis of these findings and limitations, future research should proceed in the following directions. First, studies must critically perform systematic evaluation of the homing, distribution, and therapeutic efficacy of BMSCs-Au-star in disease models with greater clinical relevance, such as bone injury, brain injury, or liver injury, and must extend the observation period to several weeks to comprehensively assess long-term tracking capability and biosafety. Second, exploring the development of multimodal probes coupled with Au-stars could achieve complementary advantages, and advanced image processing algorithms should be developed to increase quantitative accuracy. Third, a more detailed assessment of the effects of membrane modification on stem cell function from the perspectives of cellular mechanics and signal transduction is warranted. Finally, to advance the clinical translation of this technology, the synthesis and quality control standards of each component (Ac_4ManNAz and Au-star-DBCO) must be optimized, and scalable production pathways must be explored. The technological platform established in this study not only provides a powerful tool for stem cell biology research but also lays a foundation for the future development of cell-based theranostic strategies.

Conclusions

In summary, this study integrated the precision of bioorthogonal chemistry, the excellent optical properties of nanomaterials, and the deep-tissue penetration of photoacoustic imaging, to provide an efficient, specific, and versatile solution for the

dynamic tracking of stem cells in living systems. This platform is expected to not only help elucidate the *in vivo* biological behavior of transplanted stem cells but also offer a robust tool for the precise assessment of cell-based therapies. Future research should focus on addressing the stability of long-term tracking, the reliability of imaging in complex pathological environments, and systematic safety evaluation before clinical translation, to facilitate the progression of this technology from basic research to clinical application.

Data availability statement

Data generated or analyzed during this study are available from the corresponding author on request.

Ethics statement

All animal procedures were approved by the ethics committee of the Guangdong Second Provincial General Hospital (animal ethics ID: 2025-DW-KZ-116-01).

Author contributions

The authors confirm the following contributions to the article. Study conception and design: Renhao Xu, Yanni He, Hongmei Liu; data collection: Renhao Xu, Yanmei Cai, Xiaobin Dong, Xuezhi Wang; analysis and interpretation of results: Renhao Xu, Yanmei Cai; draft manuscript preparation: Renhao Xu, Wenyi Zheng, Ning Zhang. All authors reviewed the results and approved the final version of the manuscript.

Funding or acknowledgements

The work was financially supported by the National Natural Science Foundation of China (82371970 and 82202166), Youth S&T Talent Support Program of Guangdong Provincial Association for Science and Technology (SKXRC2025106), China Postdoctoral Science Foundation (2025M781942), Natural Science Foundation of Guangdong Province (2023A1515012664), Featured Clinical Technique of Guangzhou (2023P-TS40), Guangzhou Science and Technology Program (2023A03J0281), and Talents' Plan Foundation of Guangdong Second Provincial General Hospital (2024E003). The figures and graphical abstract were created in BioRender.

Conflict of interest

The authors declare that there are no conflicts of interest.

Supplementary material

Supplementary Material can be downloaded from https://bio-integration.org/wp-content/uploads/2026/04/bioi20260012_Supplemental.pdf.

References

[1] Roelofs AJ, McClure JJ, Hay EA, De Bari C. Stem and progenitor cells in the synovial joint as targets for regenerative therapy. Nat Rev Rheumatol 2025;21(4):211-20. [PMID: 40045009 DOI: 10.1038/s41584-025-01222-z]

[2] Hussen BM, Taheri M, Yashooa RK, Abdullah GH, Abdullah SR, et al. Revolutionizing medicine: recent developments and future prospects in stem-cell therapy. Int J Surg 2024;110(12):8002-24. [PMID: 39497543 DOI: 10.1097/JS9.0000000000002109]

[3] Wang LLW, Gao Y, Feng Z, Mooney DJ, Mitragotri S. Designing drug delivery systems for cell therapy. Nat Rev Bioeng 2024;2(11):944-59. [DOI: 10.1038/s44222-024-00214-0]

[4] Han X, Liao R, Li X, Zhang C, Huo S, et al. Mesenchymal stem cells in treating human diseases: molecular mechanisms and clinical studies. Signal Transduct Target Ther 2025;10(1):262. [PMID: 40841367 DOI: 10.1038/s41392-025-02313-9]

[5] Huang P, Luo Q, Yao L, Song Z, Wang J, et al. Acoustic manipulation and intracellular drug release promote bone marrow mesenchymal stem cells to repair articular cartilage defect. Chem Eng J 2025;526:171228. [DOI: 10.1016/j.cej.2025.171228]

[6] Lisi-Vega LE, Pievani A, García-Fernández M, Forte D, Williams TL, et al. Bone marrow mesenchymal stromal cells support translation in refractory acute myeloid leukemia. Cell Rep 2025;44(1):115151. [PMID: 39932190 DOI: 10.1016/j.celrep.2024.115151]

[7] Xu Z, Xin H, Wang Y, Xu R, He Y, et al. Ultrasound-mediated biotransfection of engineered bone marrow mesenchymal stem cells in treated bone defects through intracellular cavitation. Adv Sci (Weinh) 2025;12(40):e03196. [PMID: 40734590 DOI: 10.1002/advs.202503196]

[8] Meng Z, Tang M, Xu S, Zhou X, Zhang Z, et al. Protective effects of bone marrow mesenchymal stem cell-derived exosomes loaded cerium dioxide nanoparticle against deoxynivalenol-induced liver damage. J Nanobiotechnol 2025;23(1):215. [PMID: 40098176 DOI: 10.1186/s12951-025-03316-y]

[9] Zheng Y, Huang J, Zhu T, Li R, Wang Z, et al. Stem cell tracking technologies for neurological regenerative medicine purposes. Stem Cells Int 2017;2017(1):2934149. [PMID: 29138636 DOI: 10.1155/2017/2934149]

[10] Kim S, Ryu M, Youn HS, Park YG, Moon SH. High-precision in vivo tracking of stem cells using carbon-14 labeling: a novel quantitative approach for assessing therapeutic efficacy and safety. Beni-Suef Univ J Basic Appl Sci 2025;14(1):130. [DOI: 10.1186/s43088-025-00726-7]

[11] Nyström NN, Jin Z, Bennett ME, Zhang R, Swift MB, et al. Multiplexed ultrasound imaging of gene expression. Nat Methods 2025;22(12):2594-600. [PMID: 41254367 DOI: 10.1038/s41592-025-02825-w]

[12] Cao Z, Xu R, Zheng W, Ma L, He Y, et al. Ultrasound-activated selenium nanocarrier: bactericidal enhancement and osseointegration promotion for implant-associated infections. Adv Healthc Mater 2025;14(16):2500523. [PMID: 40344396 DOI: 10.1002/adhm.202500523]

[13] Huang Y, Yin Z, Xu R, Zheng W, Zhang Q, et al. Gas vesicle-assisted ultrasound imaging for effective anti-tumour CAR-T cell immunotherapy efficacy in mice model. Int J Nanomedicine 2025;20:4849-62. [PMID: 40259914 DOI: 10.2147/IJN.S508846]

[14] Gong Z, He Y, Zhou M, Xin H, Pan M, et al. Ultrasound imaging tracking of mesenchymal stem cells intracellularly labeled with biosynthetic gas vesicles for treatment of rheumatoid arthritis. Theranostics 2022;12(5):2370-82. [PMID: 35265215 DOI: 10.7150/thno.66905]

[15] Wang X, Cui B, Sun Q, Liu H, Liu Z. Small-molecule photoacoustic probes for *in vivo* imaging. Chem Soc Rev 2025;54(19):8809-44. [PMID: 40955581 DOI: 10.1039/d5cs00745c]

[16] Ouyang J, Xie A, Zhou J, Liu R, Wang L, et al. Minimally invasive nanomedicine: nanotechnology in photo-/ultrasound-/radiation-/magnetism-mediated therapy and imaging. Chem Soc Rev 2022;51(12):4996-5041. [PMID: 35616098 DOI: 10.1039/d1cs01148k]

[17] Kim T, Lemaster JE, Chen F, Li J, Jokerst JV. Photoacoustic imaging of human mesenchymal stem cells labeled with Prussian blue–poly(l-lysine) Nanocomplexes. ACS Nano 2017;11(9):9022-32. [PMID: 28759195 DOI: 10.1021/acsnano.7b03519]

[18] Qiyami Hour F, Shabani R, Ashtari B, Moinzadeh A, Mehdizadeh M. Labelling of human Wharton's jelly-derived mesenchymal stem cells with gold nanorods by biomimicry method. Cell Biochem Funct 2021;39(8):983-90. [PMID: 34374101 DOI: 10.1002/cbf.3665]

[19] Salah D, Moghanm FS, Arshad M, Alanazi AA, Latif S, et al. Polymer-peptide modified gold nanorods to improve cell conjugation and cell labelling for stem cells photoacoustic imaging. Diagnostics (Basel) 2021;11(7):1196. [PMID: 34209370 DOI: 10.3390/diagnostics11071196]

[20] Meng H, Cheng S, Wang L, Balachandran YL, Zhang W, et al. Large-scale production of Au nanoparticles as medical antibiotics. Mater Adv 2022;3(22):8137-40. [DOI: 10.1039/D2MA00713D]

[21] Meng H, Yu Q, Liu Z, Gai Y, Xue J, et al. Triboelectric performances of biodegradable polymers. Matter 2023;6(12):4274-90. [DOI: 10.1016/j.matt.2023.09.017]

[22] Zhang R, Thoröe-Boveleth S, Chigrin DN, Kiessling F, Lammers T, et al. Nanoscale engineering of gold nanostars for enhanced photoacoustic imaging. J Nanobiotechnol 2024;22(1):115. [PMID: 38493118 DOI: 10.1186/s12951-024-02379-7]

[23] Miao Y, Wang Y, Chen Y, Huang Z, Lu C, et al. Pretargeted multimodal tumor imaging by enzymatic self-immobilization labeling and bioorthogonal reaction. J Am Chem Soc 2025;147(3):2809-21. [PMID: 39801138 DOI: 10.1021/jacs.4c15896]

[24] Laporte AAH, Reek JNH. Supramolecular materials and strategies for bioorthogonal chemical transformations. Chem Rev 2025;125(15):7223-74. [PMID: 40748820 DOI: 10.1021/acs.chemrev.5c00047]

[25] Pan H, Li WJ, Yao XJ, Wu YY, Liu LL, et al. In situ bioorthogonal metabolic labeling for fluorescence imaging of virus infection in vivo. Small 2017;13(17):1604036. [PMID: 28218446 DOI: 10.1002/smll.201604036]

[26] Zheng W, Ma L, Luo X, Xu R, Cao Z, et al. Ultrasound-triggered functional hydrogel promotes multistage bone regeneration. Biomaterials 2024;311:122650. [PMID: 38889598 DOI: 10.1016/j.biomaterials.2024.122650]

[27] Xu R, You Y, Zheng W, Ma L, Chang Y, et al. Selenoprotein-regulated hydrogel for ultrasound-controlled microenvironment remodeling to promote bone defect repair. Adv Funct Mater 2024;34(12):2313122. [DOI: 10.1002/adfm.202313122]

[28] Chen Y, Xu R, Xie B, Ma L, He Y, et al. Ultrasound-driven selenium nanoparticles realize bone defect repair through activating selenoproteins to regulate PI3K/AKT signaling pathway. ACS Nano 2025;19(19):18256-69. [PMID: 40338671 DOI: 10.1021/acsnano.4c18240]

[29] Ni X, Jia S, Duan X, Ding D, Li K. Fluorescent nanoparticles for noninvasive stem cell tracking in regenerative medicine. J Biomed Nanotechnol 2018;14(2):240-56. [PMID: 31352921 DOI: 10.1166/jbn.2018.2502]

[30] Jain S, Bhatt J, Gupta S, Bhatia DD. Nanotechnology at the crossroads of stem cell medicine. Biomater Sci 2025;13(1):161-78. [DOI: 10.1039/D4BM01257G]

[31] José Sánchez M, Leivar P, Borrós S, Fornaguera C, Lecina M. Enhanced quantification and cell tracking of dual fluorescent labeled extracellular vesicles. Int J Pharm 2024;667(Pt A):124921. [PMID: 39521157 DOI: 10.1016/j.ijpharm.2024.124921]

[32] Jalli R, Mehrabani D, Zare S, Saeedi Moghadam M, Jamhiri I, et al. Cell Proliferation, viability, differentiation, and apoptosis of iron oxide labeled stem cells transfected with lipofectamine assessed by MRI. J Clin Med 2023;12(6):2395. [PMID: 36983399 DOI: 10.3390/jcm12062395]

[33] Lee S, Yoon HI, Na JH, Jeon S, Lim S, et al. *In vivo* stem cell tracking with imageable nanoparticles that bind bioorthogonal chemical receptors on the stem cell surface. Biomaterials 2017;139:12-29. [PMID: 28582715 DOI: 10.1016/j.biomaterials.2017.05.050]